

An Impact of Switching Frequency and Model Accuracy on Model Predictive Current Control Performance for Reluctance Synchronous Motors

Research paper

Robert Surus*^{ORCID}, Mateusz Tejer^{ORCID}, Tomasz Tarczewski^{ORCID}

Institute of Engineering and Technology, Nicolaus Copernicus University in Toruń, ul. Wileńska 7, Toruń, Poland

Received: 26 December 2023; Accepted: 26 January 2024

Abstract: The present paper investigates the feasibility of utilizing the simplified prediction model for finite control set model predictive current control (FCS-MPCC) applied to reluctance synchronous motors (RSMs). The FCS-MPCC exhibits torque and current ripples, and a crucial consideration is the reduction of these ripples by increasing the switching frequency. The algorithm's computational complexity is tied to the accuracy of the adopted model. Two approaches with varying levels of accuracy in predicting current dependencies concerning changes in the inductance of the RSM are investigated. The findings highlight the potential of employing simplified fixed inductance values for efficient control in drive systems, particularly those amenable to high switching frequencies.

Keywords: *model predictive current control • reluctance synchronous motor • switching frequency • torque and current ripples*

1. Introduction

AC motors are renowned for their exceptional energy efficiency (Awan et al., 2019; Boldea and Tutelea 2018). These motors can be categorised into three main types: permanent magnet synchronous motors (PMSMs), induction motors (IMs) and reluctance synchronous motors (RSMs). Notably, RSMs offer key advantages, such as reduced vibration, superior energy efficiency and a more cost-effective solution due to the absence of permanent magnets, distinguishing them from PMSMs and IMs (Awan et al. 2019). The inherent construction of the RSM introduces are contingent on current levels, achieving precise control over speed and torque and this necessitates the development of a precise mathematical model. RSMs find applications in electric vehicles and heating, ventilation, air conditioning systems (ABB white paper). Due to resemblance in the stator construction of RSM, PMSM and IM, it is feasible to employ a cascade control structure (CCS) utilising a field-oriented control (FOC) strategy (Boldea and Tutelea, 2018). However, it is essential to note that this approach has a notable drawback, mainly associated with limited bandwidth, which leads to relatively modest speed control dynamics. Instead of the conventional CCS various alternatives such as a state feedback controller (SFC) (Niedworok and Orzech, 2016; Tarczewski et al., 2021a,b), a sliding mode control (Manuel and Inanc, 2022; Zhang et al., 2013) and model predictive control (MPC) (Fahran et al. 2020; Wang et al., 2017) can be employed. When distinguishing between different types of MPC, we can classify them into two primary categories: finite control set MPC (FCS-MPC) and continuous set MPC (CS-MPC) (Wróbel et al. 2020). Due to its high performance, rapid response, and straightforward computational requirements, FCS-MPC holds promise as an effective approach for RSMs. In this context, the control signals' values are derived through an optimisation procedure to minimise a specific cost function. Consequently, the optimal voltage vector is

* Email: rsurus@umk.pl

established for a given time horizon and subsequently employed to control the switching of the inverters' transistors. This particular control structure operates without the need for a space vector modulator (SVM) and involves a reduced set of parameters when compared to an FOC structure.

This paper explores applying a finite control set - model predictive current control (FCS-MPCC) for RSM, focusing on the advantages of drive systems capable of operating at high switching frequencies and highlighting the benefits of a simplified model approach in this context. The research delves into the impact of switching frequency on torque and current ripples, considering models with varying levels of accuracy. Emphasising the potential benefits of drives accommodating high frequencies is aimed to pave the way for simplified models. Additionally, the tests at a higher switching frequency were conducted to assess the influence of changes in inductance on the performance of the drive system.

2. Mathematical Model of Drive

The RSM control is implemented within a rotating reference frame (RRF) coordinate system, necessitating the mathematical model to be established regarding the D- and Q- axes components of flux linkage and current (Niewiara et al., 2023a,b). The RSM model can be described by the following equations:

$$\frac{d\psi_d(t)}{dt} = u_{sd}(t) - Ri_{sd}(t) + p\omega_m(t)\psi_q(t) \quad (1)$$

$$\frac{d\psi_q(t)}{dt} = u_{sq}(t) - Ri_{sq}(t) - p\omega_m(t)\psi_d(t) \quad (2)$$

$$J\frac{d\omega_m(t)}{dt} = \frac{3}{2}p(\psi_d(t)i_{sq}(t) - \psi_q(t)i_{sd}(t)) - B\omega_m(t) - T_L(t) \quad (3)$$

$$\psi_d(t) = L_d(i_{sd}(t), i_{sq}(t))i_{sd}(t) \quad (4)$$

$$\psi_q(t) = L_q(i_{sd}(t), i_{sq}(t))i_{sq}(t) \quad (5)$$

where: $u_{sd}(t)$ and $u_{sq}(t)$ is the input voltages given in RRF, $i_{sd}(t)$ and $i_{sq}(t)$ is the stator current components given in RRF, $\psi_d(t)$ and $\psi_q(t)$ is the magnetic flux components, R is a stator resistance, p is a number of pole pairs, $\omega_m(t)$ is a rotational velocity of the rotor, J is a moment of inertia, B is a viscous friction coefficient and $T_L(t)$ is a load torque.

Considering that the linked fluxes are contingent on the stator current components, the derivative of these fluxes can be expressed in the following dependencies:

$$\frac{d\psi_d(i_{sd}, i_{sq})(t)}{dt} = \frac{\partial\psi_d(i_{sd}, i_{sq})(t)}{\partial i_{sd}} \frac{di_{sd}(t)}{dt} + \frac{\partial\psi_d(i_{sd}, i_{sq})(t)}{\partial i_{sq}} \frac{di_{sq}(t)}{dt} \quad (6)$$

$$\frac{d\psi_q(i_{sd}, i_{sq})(t)}{dt} = \frac{\partial\psi_q(i_{sd}, i_{sq})(t)}{\partial i_{sd}} \frac{di_{sd}(t)}{dt} + \frac{\partial\psi_q(i_{sd}, i_{sq})(t)}{\partial i_{sq}} \frac{di_{sq}(t)}{dt} \quad (7)$$

Taking into account Eq. (4) and (5), Eq. (6) and (7) are obtained, respectively:

$$L_{dd}(i_{sd}(t), i_{sq}(t)) = L_d(i_{sd}(t), i_{sq}(t)) + \frac{\partial L_d(i_{sd}(t), i_{sq}(t))}{\partial i_{sd}} i_{sd}(t) \quad (8)$$

$$L_{dq}(i_{sd}(t), i_{sq}(t)) = \frac{\partial L_d(i_{sd}(t), i_{sq}(t))}{\partial i_{sq}} i_{sd}(t) \quad (9)$$

$$L_{qd}(i_{sd}(t), i_{sq}(t)) = \frac{\partial L_q(i_{sd}(t), i_{sq}(t))}{\partial i_{sd}} i_{sq}(t) \quad (10)$$

$$L_{qq}(i_{sd}(t), i_{sq}(t)) = L_q(i_{sd}(t), i_{sq}(t)) + \frac{\partial L_q(i_{sd}(t), i_{sq}(t))}{\partial i_{sq}} i_{sq}(t) \quad (11)$$

By employing an identification approach that indirectly measures the magnetic fluxes linked to the stator current components, it becomes possible to ascertain four elements of the motor inductances. One viable method for establishing inductance surfaces involves polynomial approximation within the MATLAB environment (Niewiara et al., 2023a,b; Yamamoto et al., 2018). It is important to note that due to the magnetic saturation effects, the D- and Q-axes components of inductance exhibit pronounced non-linearity and are influenced by the current (Yamamoto et al., 2005). It should be noted, however, that identifying the inductance as a function of currents is a time-consuming process, and implementing the approximated relationships requires using a microcontroller with more significant computational resources. Moreover, the considered approach has to be repeated for all machines separately due to possible parameter fluctuations (Wang and Zhang, 2021). Therefore, it seems to be justified to verify the application of a simplified model in the prediction control scheme.

3. Control Structure

The proposed control framework is based on a cascade configuration, incorporating both the angular velocity controller and the model predictive current control (MPCC) structures. As illustrated in Figure 1, implementing the Maximum Torque Per Ampere (MTPA) strategy has been adopted to improve the efficiency of the RSM (Mahmoud et al., 2018; Surus et al., 2022). The velocity controller's output sets the reference torque for the MTPA module. A proportional-integral (PI) controller was employed to control angular velocity, with coefficients determined using the Ziegler Nichols second criterion. The complete block diagram of the control arrangement is presented in Figure 1.

To use the FCS-MPCC scheme, it is crucial to establish a suitable cost function and an associated discrete predictive model for the electrical characteristics of the RSM. In this approach, the following cost function was utilised:

$$g = \sum_{n=1}^N \left((i_{dref}(k+n) - i_{sdp}(k+n))^2 + (i_{qref}(k+n) - i_{sqp}(k+n))^2 \right) \quad (12)$$

where: $i_{dref}(k+n)$ and $i_{qref}(k+n)$ are the reference rotor and stator current components in next moment of time, $i_{sdp}(k+n)$ and $i_{sqp}(k+n)$ are the predictive rotor and stator current components in next moment of time, N is the prediction horizon. It should be noted that the considered cost function does not contain the weighting coefficients to be selected.

The overarching objective throughout the process is to reduce the values of the cost function. By minimising this cost function, appropriate voltage vectors were derived. The Euler discretisation was applied to Eqs. (1)-(5) to obtain the discrete current-prediction model. In each prediction step, seven distinct voltage vectors are

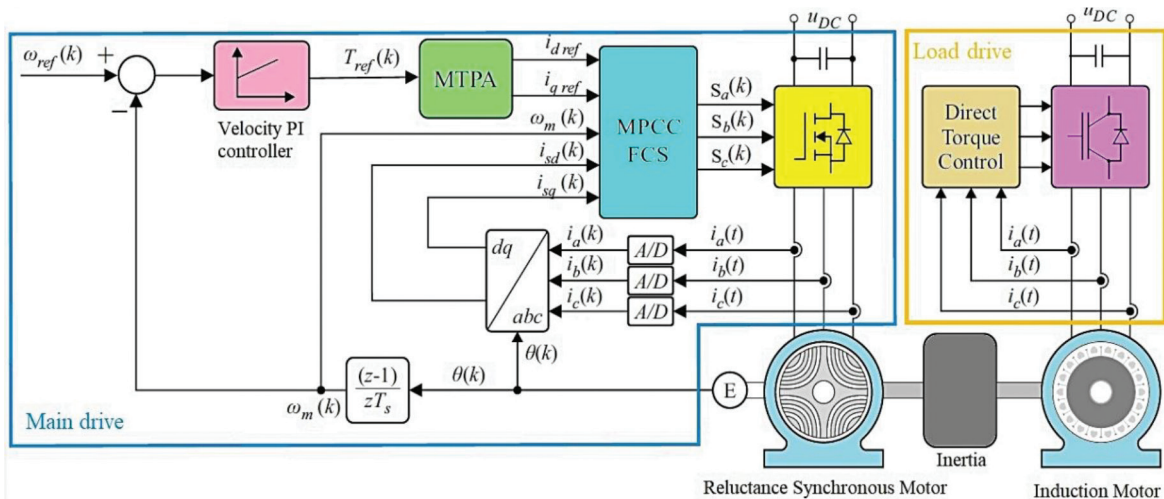


Fig. 1. Block diagram of the PI-MTPA-FCS-MPCC control structure for RSM.

Table 1. Voltage vectors for FCS-MPCC

Conducting modes	Switching states	Output Voltages
	S_a, S_b, S_c	V_α, V_β
u_0	0 0 0	0, 0
u_1	1 0 0	$\frac{2}{3}V_{dc}, 0$
u_2	1 1 0	$\frac{1}{3}V_{dc}, \frac{\sqrt{3}}{3}V_{dc}$
u_3	0 1 0	$-\frac{1}{3}V_{dc}, \frac{\sqrt{3}}{3}V_{dc}$
u_4	0 1 1	$\frac{1}{3}V_{dc}, 0$
u_5	0 0 1	$-\frac{1}{3}V_{dc}, -\frac{\sqrt{3}}{3}V_{dc}$
u_6	1 0 1	$\frac{1}{3}V_{dc}, -\frac{\sqrt{3}}{3}V_{dc}$
u_7	1 1 1	0, 0

utilised, corresponding to the seven different switching states of the inverter, as categorised in Table 1 within the stationary reference frame $\alpha\beta$. To prevent the duplication of the cost function values and to reduce the algorithm's computational complexity, one zero vector was used. Then, the Park transformation is applied to convert these voltages into RRF.

The relationship between the prediction horizon and the number of potential cost functions follows an exponential pattern:

$$m = 7^N \quad (13)$$

where m is the number of possible cost function values. The computational complexity of the standard MPCC approach is high (Surus et al., 2023). Therefore, it was decided to analyse strategies that enable reducing the computational complexity of the algorithm.

3.1. FCS-MPCC-1 – Model with all variable inductance components

In the first approach of the MPCC methodology, the inclusion of all the components of the RSM inductances $L_{dd}, L_{dq}, L_{qd}, L_{qq}$ and L_d, L_q reliant on the currents $i_{sd}(t), i_{sq}(t)$ is taken into account. Using the inductance components L_d and L_q allows obtaining superficial relationships describing the electromotive force while maintaining the four inductance components $L_{dd}, L_{dq}, L_{qd}, L_{qq}$ in the considered model compared to solution, presented in Surus et al., (2023). The discrete formulas that describe predictive currents of the RSM take the following form:

$$\begin{bmatrix} i_{sdp}^{MPCC1}(k+1) \\ i_{sqp}^{MPCC1}(k+1) \end{bmatrix} = \begin{bmatrix} i_{sd}(k) \\ i_{sq}(k) \end{bmatrix} + T_s L^{-1} \left(-R \begin{bmatrix} i_{sd}(k) \\ i_{sq}(k) \end{bmatrix} + p\omega_m(k) \begin{bmatrix} L_d(i_{sd}(k), i_{sq}(k)) \\ L_q(i_{sd}(k), i_{sq}(k)) \end{bmatrix} \begin{bmatrix} i_{sd}(k) \\ i_{sq}(k) \end{bmatrix} + \begin{bmatrix} u_{sd}(k) \\ u_{sq}(k) \end{bmatrix} \right) \quad (14)$$

where: T_s is a sampling period, $i_{sd}(k), i_{sq}(k)$ are measured RRF current components and L is an array of inductance components.

$$L = \begin{bmatrix} L_{dd}(i_{sd}(k), i_{sq}(k)) & L_{dq}(i_{sd}(k), i_{sq}(k)) \\ L_{qd}(i_{sd}(k), i_{sq}(k)) & L_{qq}(i_{sd}(k), i_{sq}(k)) \end{bmatrix} \quad (15)$$

Examining Eq. (14) it becomes evident that the most accuracy MPCC for RSM model is quite intricate, leading to an anticipation of substantial requirement for computational resources (Surus et al., 2023).

3.2. FCS-MPCC-2 – Model with fixed inductances in the RSM model

To investigate the impact of the RSM model accuracy on the control performance and algorithm complexity, simplification of the model has been proposed. Variable inductance components (14) and (15) were replaced by fixed values. In the result, the predicted current equations are as follows:

$$i_{sdp}^{MPCC2}(k+1) = \left(1 - \frac{T_s R}{L_{df}}\right) i_{sd}(k) + T_s \frac{L_{df}}{L_{df}} p \omega_m(k) i_{sq}(k) + \frac{T_s u_{sd}(k)}{L_{df}} \quad (16)$$

$$i_{sqp}^{MPCC2}(k+1) = \left(1 - \frac{T_s R}{L_{df}}\right) i_{sq}(k) + T_s \frac{L_{df}}{L_{df}} p \omega_m(k) i_{sd}(k) + \frac{T_s u_{sq}(k)}{L_{df}} \quad (17)$$

where: L_{df} and L_{df} are fixed inductances. FCS-MPCC-2 allows reducing the computational complexity of the algorithm and extending the prediction horizon (Scokaert and Mayne, 1998; Surus et al., 2023). The advantage of the solution is that there is no need to determine inductance surfaces in the identification process. However, the information about average inductance values is most often proprietary to drive system manufacturers. These values can be determined from geometric and material parameters of the RSM (Boldea and Tutelea, 2018) or by using the LCR meter (Kumar et al., 2020). Another way to determining the averaged inductance values is using load drive. The motor shaft is rotated by the load drive at a constant velocity and a step change in voltage to generate the electromotive force in the RSM. In the steady state, the averaged currents \bar{i}_{sd} and \bar{i}_{sq} , velocity $\bar{\omega}_m$ and the voltages \bar{u}_{sd} and \bar{u}_{sq} can be used to determine the averaged inductance values (Niewiara et al. 2023a,b).

$$\bar{\psi}_d = \frac{\bar{u}_{sq} - R \bar{i}_{sq}}{p \bar{\omega}_m} \quad (18)$$

$$\bar{\psi}_q = \frac{\bar{u}_{sd} - R \bar{i}_{sd}}{p \bar{\omega}_m} \quad (19)$$

$$L_{df} = \frac{\bar{\psi}_d}{\bar{i}_{sd}} \quad (20)$$

$$L_{df} = \frac{\bar{\psi}_q}{\bar{i}_{sq}} \quad (21)$$

where $\bar{\psi}_d$ and $\bar{\psi}_q$ are the averaged fluxes in RRF.

4. An Impact of Model Complexity on the Predictive Control Performance

4.1. The differences between prediction currents

Since microcontrollers have limited computational resources when implementing complex control algorithms, to reduce the computational complexity of the FCS-MPCC algorithm, a simplified model that ignores the non-linear inductance characteristics, can be adopted. However, the accuracy of the adopted model, may significantly affect the performance of the control system. Adopting the most accurate model (FCS-MPCC-1) when implementing the algorithm, translates into obtaining more accurate values of prediction currents. If the simplified model (FCS-MPCC-2) is used to implement the FCS-MPCC algorithm, obtaining the slightest difference between the prediction currents obtained in individual models is essential. Numerical tests were performed in Matlab to determine the maximum differences between the prediction currents of the two presented models. The tests were carried out for various values of currents i_{sd} and i_{sq} , switching frequency and velocity values. In Figure 2 the characteristics of the maximum differences between the predicted currents obtained in FCS-MPCC-1 and FCS-MPCC-2 depending on the currents for two switching frequencies are presented. The relationship between the prediction currents for individual components in the RRF can be presented as:

$$\Delta i_{dp} = i_{sdp}^{MPCC1}(k+1) - i_{sdp}^{MPCC2}(k+1) \quad (22)$$

$$\Delta i_{qp} = i_{sqp}^{MPCC1}(k+1) - i_{sqp}^{MPCC2}(k+1) \quad (23)$$

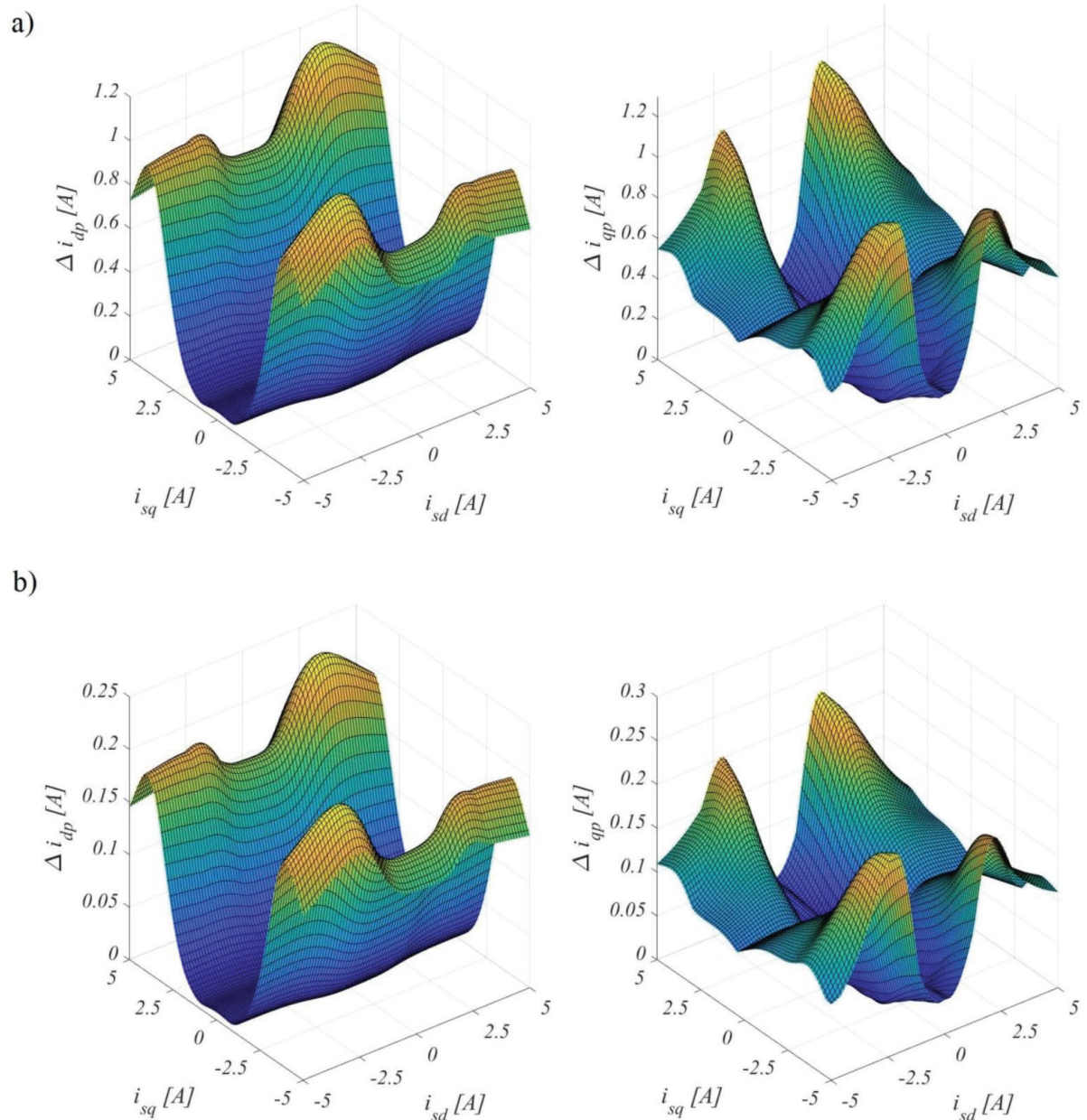


Fig. 2. The characteristics of the maximum differences between the prediction currents in FCS-MPCC-1 and FCS-MPCC-2 as a function of currents for (a) switching frequency 5kHz (b) switching frequency 25kHz and rotational velocity 500 rpm.

It was observed that the lowest values of maximum differences between prediction currents occur for low values of measured currents. As the value of the currents increases, the difference between the prediction currents increases, translating into different values of the minimum cost function and determining the optimal voltage vector. An increase in the value of measured currents appears during transient states of velocity or the applied load torque. Using an inverter with metal-oxide-semiconductor field-effect transistors which are made of silicon carbide (SiC-MOSFET), the switching frequency can be increased to higher values and the maximum difference between the prediction currents in FCS-MPCC-1 and FCS-MPCC-2 can be reduced. Increasing the switching frequency from 5kHz to 25kHz makes it possible to reduce the maximum differences between the prediction currents by 0.93A for both current components. In Table 2 the values of the maximum differences between the prediction currents for two switching frequencies are presented.

In Figure 3 the differences in prediction currents in FCS-MPCC-1 and FCS-MPCC-2 depending on switching frequency and velocity are presented.

Table 2. Values of maximum differences between prediction currents for two switching frequencies

f_s [kHz]	Δi_{dp}^{max} [A]	Δi_{qp}^{max} [A]
5	1.16	1.15
25	0.23	0.22

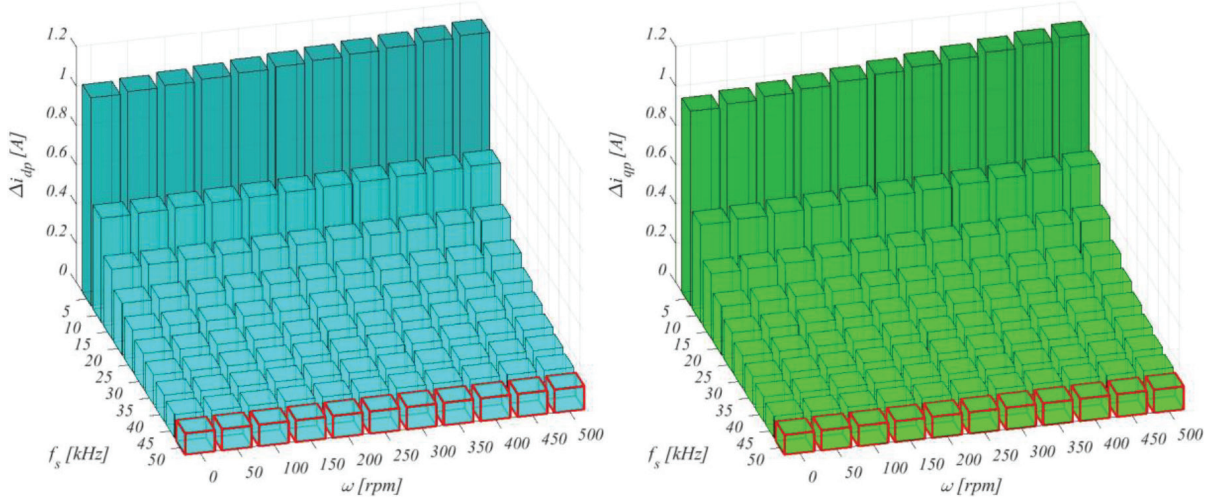


Fig. 3. The characteristics of the differences between the prediction currents in FCS-MPCC-1 and FCS-MPCC-2 as a function of rotational velocity and switching frequency.

Based on results in Figures 2 and 3 it can be concluded that increasing the switching frequency makes it possible to reduce the difference between the prediction currents. The angular velocity has a negligible impact on the prediction currents inaccuracy.

5. Experimental Setup, Results and Analysis

The experimental test-bed is shown in Figure 4. It consists of an RSM, (3GAL092513-ASB) with a control unit, load drive with IM (3GAA092214-ASE), both manufactured by ABB and two clutches. To simulate a working machine, an additional inertia was introduced. The RSM control unit is based on a SiC-MOSFET power module and a NXP MKV58F1M0VLL24 microcontroller. The main parameters of the laboratory setup are listed in Table 3.

The decision was made to validate the suggested MPCC methodologies through experimental tests conducted on a self-developed prototype of a voltage source inverter (VSI). Due to the limited computational resources of the microcontroller, experimental studies were carried out for the prediction horizon equal to 1 and five different switching frequencies for both considered control schemes. The RSM torque is calculated, based on the recorded current components. Compensation for the measurement delay must be introduced to ensure the correct operation of the algorithm. The current and speed control algorithms are covered by changing the switching frequency. The relationships for predictive currents contain in a discrete form the sampling period in each proposed solution. To compare the performance of proposed control systems in terms of torque and current ripple, the following quality indicators were used.

$$T_e^{ACRMS} = \sqrt{\frac{1}{t_r} \int_{t-t_r}^t (T_e(t) - T_e^{AVG})^2 dt} \quad (24)$$

$$i_{sd}^{ACRMS} = \sqrt{\frac{1}{t_r} \int_{t-t_r}^t (i_{sd}(t) - i_{sd}^{AVG})^2 dt} \quad (25)$$

$$i_{sq}^{ACRMS} = \sqrt{\frac{1}{t_r} \int_{t-t_r}^t (i_{sq}(t) - i_{sq}^{AVG})^2 dt} \quad (26)$$



Fig. 4. The experimental setup with RSM drive and IM load drive.

Table 3. Parameters of the RSM drive

Parameter name	Symbol	Value	Unit
DC-link voltage	U_{dc}	450	V
Rated current	I_N	2.9	A
Rated torque	T_N	7.0	Nm
Rated velocity	N_N	1500	rpm
Rated power	P_N	1.1	kW
Stator resistance	R	6.0	Ω
Number of pole pairs	p	2	-
Moment of inertia (summarized)	J	0.011	kgm ²
Viscous friction coefficient	B	0.015	Nms/rad

Table 4. The root mean square values of torque and currents ripples for the two approaches FCS-MPCC

f [kHz]	FCS-MPCC-1			FCS-MPCC-2		
	ΔT_e^{ACRMS} [Nm]	Δi_{sd}^{ACRMS} [A]	Δi_{sq}^{ACRMS} [A]	ΔT_e^{ACRMS} [Nm]	Δi_{sd}^{ACRMS} [A]	Δi_{sq}^{ACRMS} [A]
5	1.51	0.19	0.65	1.97	0.19	0.70
10	0.51	0.07	0.22	0.86	0.08	0.30
15	0.15	0.04	0.07	0.40	0.07	0.09
20	0.14	0.03	0.05	0.33	0.05	0.08
25	0.12	0.03	0.05	0.23	0.03	0.07

where T_e^{AVG} , i_{sd}^{AVG} , i_{sq}^{AVG} are the averaged values of the torque ripples and current components in the D- and Q- axes, t_r is the rotor rotation period. Based on the indicators mentioned above, the effectiveness of the control systems can be compared (Jackiewicz, 2023) and shown in Table 4. Results of the experimental tests are presented in Figures 5-7.

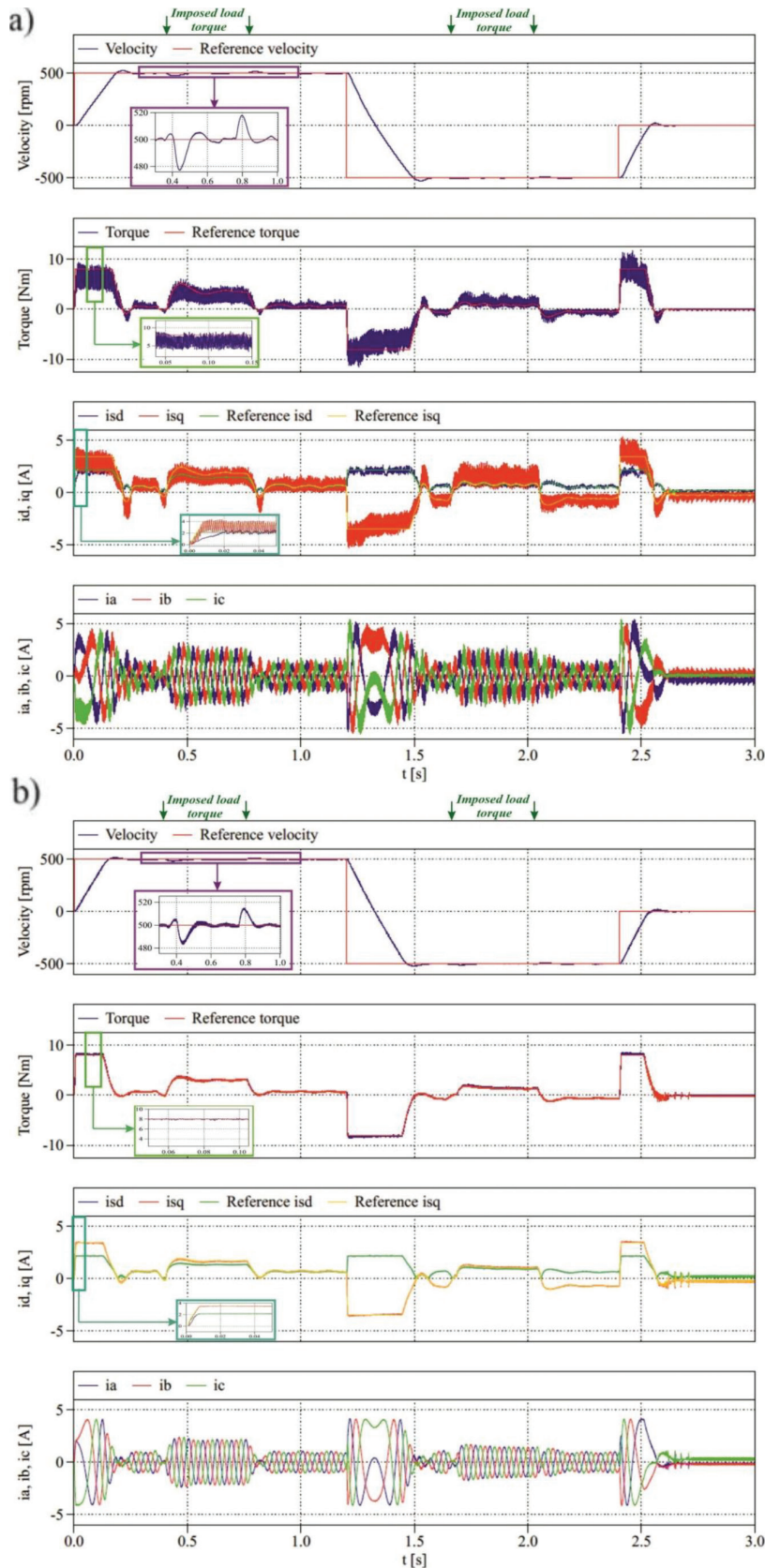


Fig. 5. Experimental results for the velocity step response under load operation with the proposed FCS-MPCC-1 strategy for switching frequency (a) 5kHz and (b) 25kHz.

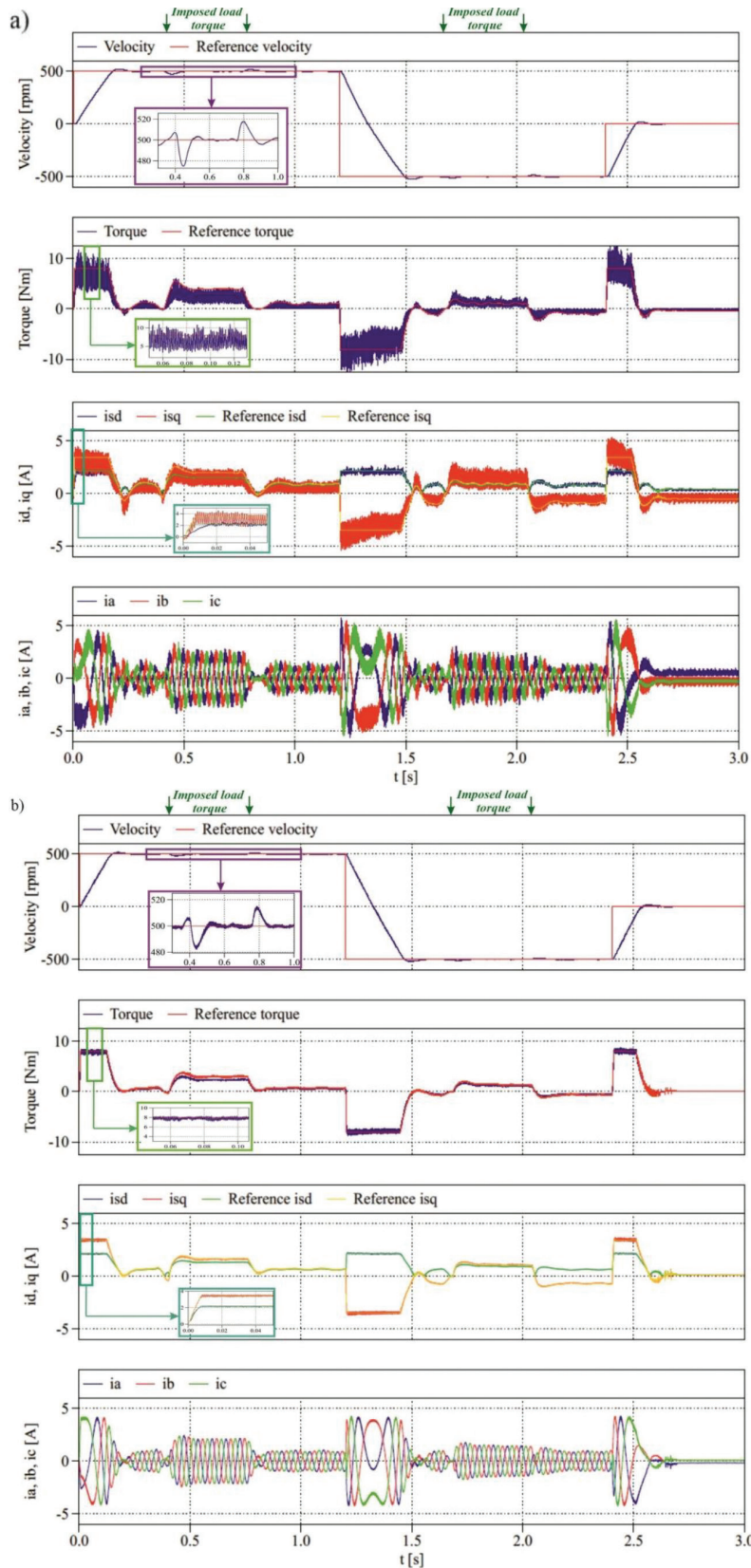


Fig. 6. Experimental results for the velocity step response under load operation with the proposed FCS-MPCC-2 strategy for switching frequency (a) 5kHz and (b) 25kHz.

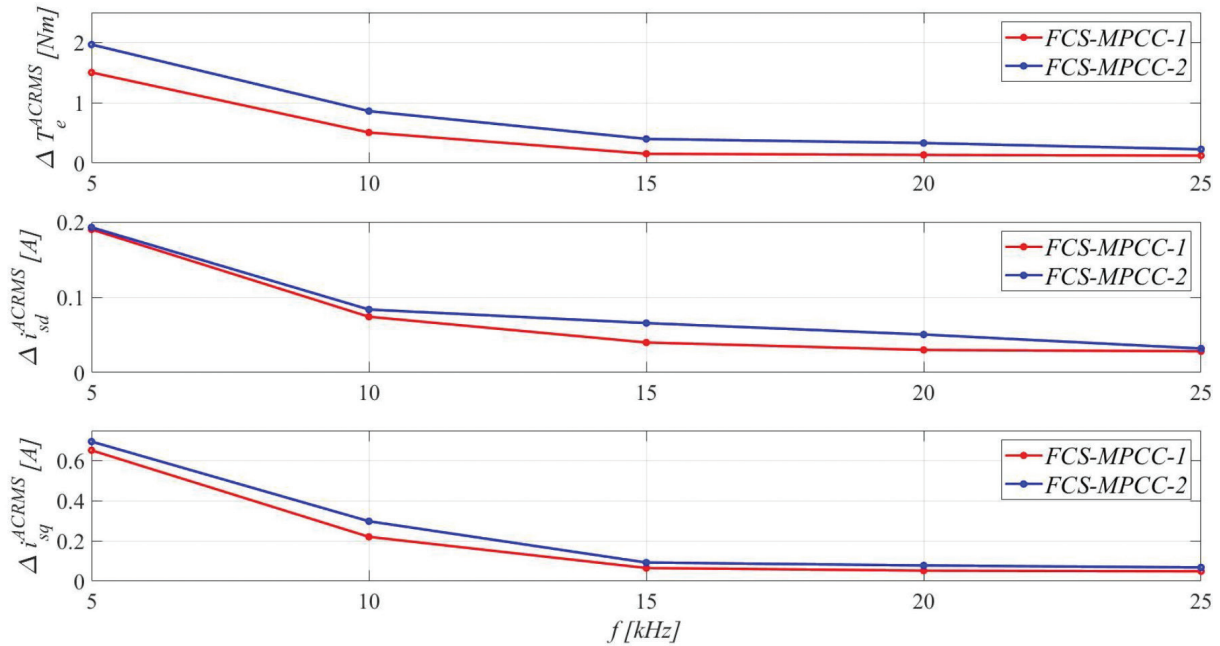


Fig. 7. The characteristics of the root mean square value of torque and current ripples as a function of switching frequency.

Adequate control of the angular velocity is observed across all examined methodologies and switching frequencies. For each of the tested models and sampling frequencies, the i_{sd} current component reaches a positive value regardless of direction of rotation of the motor shaft. This behaviour confirms that the MTPA strategy is working correctly. For each proposed solution, a well-compensated imposed load torque was observed. For a switching frequency of 25kHz, the velocity ripples are higher than for a switching frequency of 5kHz, for both considered models. Then, the experimental tests were conducted when the inductance values were reduced by 50% and 75% for each proposed model. Reducing the inductance value increased the current and torque ripple values. Results of the experimental tests are presented in Figures 8 and 9 and Table 5.

6. Conclusion

In this paper, the FCS model predictive current control for RSM, was presented, focusing on the impact of switching frequency on the control algorithm's performance. It was observed that the increased switching frequency correlates with reduced differences between predicted and actual currents, leading to diminished torque and current ripples across all considered approaches. Notably, at a switching frequency of 25kHz, comparable levels of torque and current ripples were evident in each proposed solution. The findings underscore the adaptability of the control algorithm to limited computational resources, allowing for adoption of a simplified control algorithm. Leveraging this, increasing the switching frequency was demonstrated as an effective strategy to enhance the drive system's efficiency while concurrently reducing the amplitude of current and torque ripples. Future work will involve algorithm optimisation to extend the prediction horizon for the FCS-MPCC-1. The proposed solutions were also tested at higher sampling frequencies, reaffirming the potential advantages of utilising fixed inductance values determined through simplified methods or provided by the manufacturer. This research aligns to establish the practicality and benefits of simplified models in the FCS-MPCC for RSMs operating at elevated switching frequencies. Future research aims to modify the cost function to obtain a similar or lower level of current ripple and torque as for switching frequencies 10kHz and 25kHz at low switching frequencies.

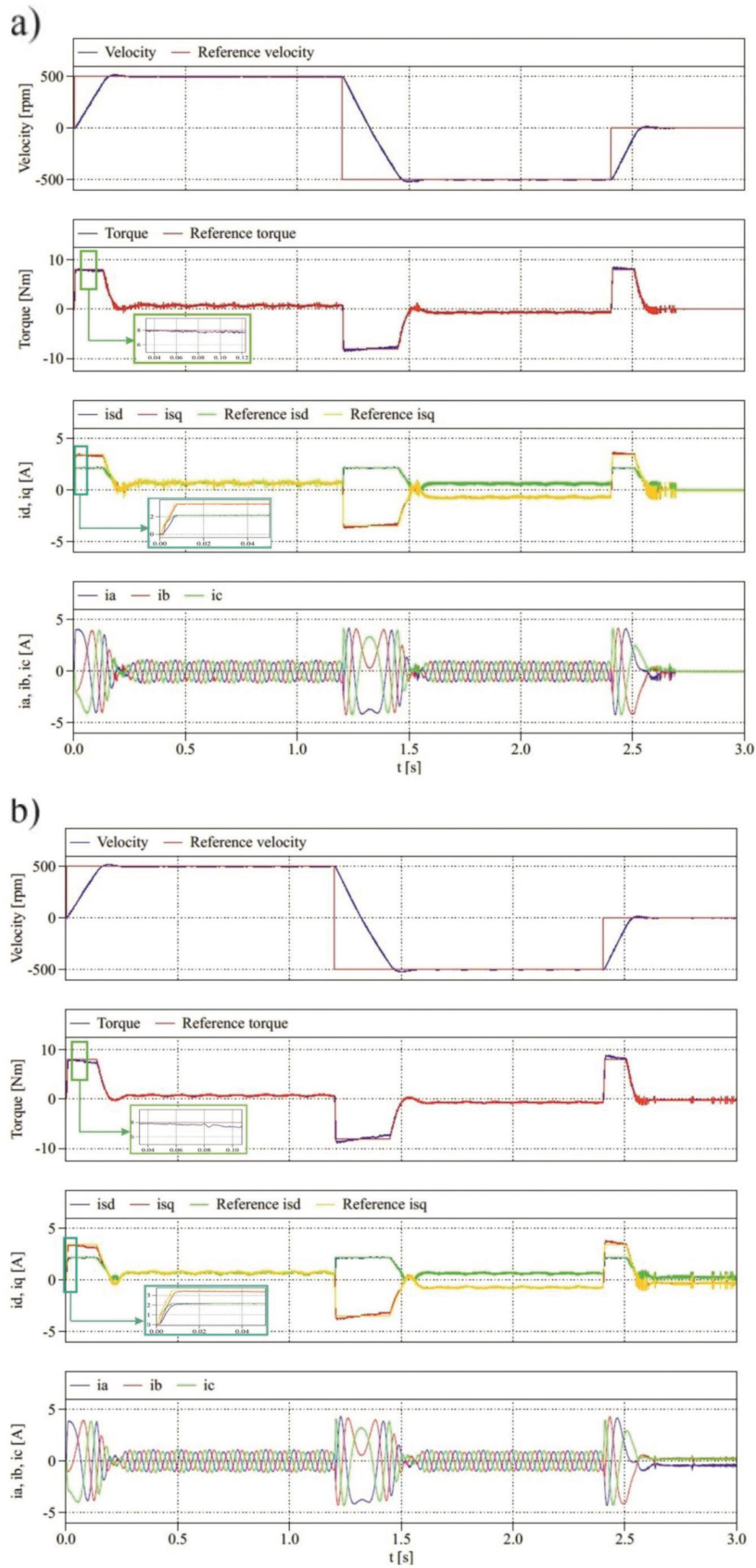


Fig. 8. Experimental results for the velocity step response with the proposed FCS-MPCC-1 strategy for switching frequency 25kHz and (a) 50% full values of inductances and (b) 75% full values of inductances.

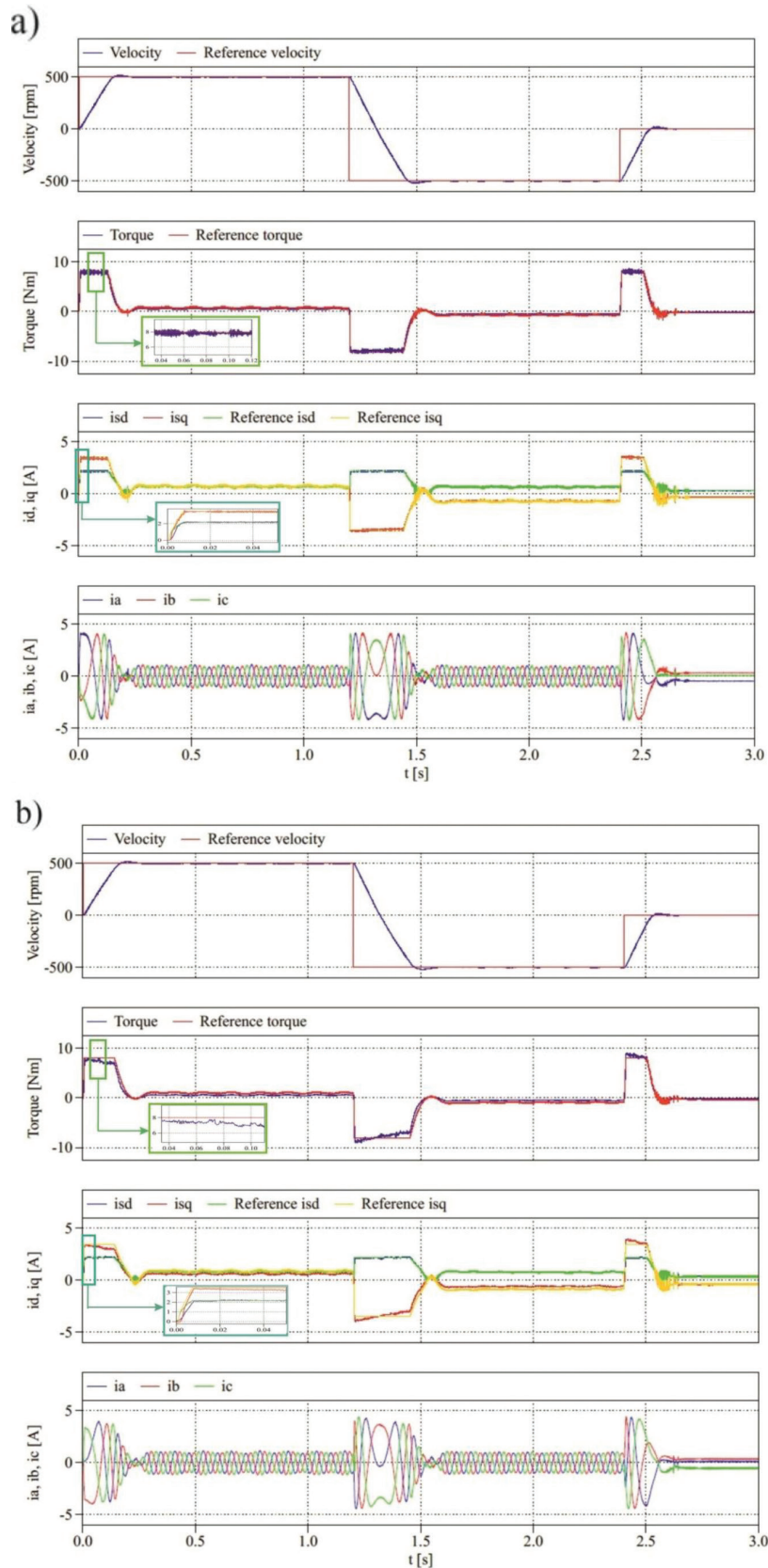


Fig. 9. Experimental results for the velocity step response with the proposed FCS-MPCC-2 strategy for switching frequency 25kHz and a) 50% full values of inductances and b) 75% full values of inductances.

Table 5. The root mean square values of torque and current ripples for the two approaches FCS-MPCC and lower values of inductances.

L [%]	FCS-MPCC-1			FCS-MPCC-2		
	ΔT_e^{ACRMS} [Nm]	Δi_{sd}^{ACRMS} [A]	Δi_{sq}^{ACRMS} [A]	ΔT_e^{ACRMS} [Nm]	Δi_{sd}^{ACRMS} [A]	Δi_{sq}^{ACRMS} [A]
50	0.21	0.04	0.08	0.38	0.08	0.12
75	0.15	0.03	0.06	0.30	0.06	0.10
100	0.12	0.03	0.05	0.23	0.03	0.07

References

- Awan, H.A.A., Saarakkala, S.E. and Hinkkanen, M., (2019) "Flux-Linkage-Based Current Control of Saturated Synchronous Motors," *IEEE Trans. Ind. Applicat.*, vol. 55, no. 5, pp. 4762–4769, doi: 10.1109/TIA.2019.2919258.
- Boldea, I. and Tutelea, L. (2018) "Reluctance Electric Machines: Design and Control", CRC Press, Taylor & Francis Group
- Farhan, A., Abdelrahem, M., Saleh, A., Shaltout, A. and Kennel, R. (2020) "Simplified Sensorless Current Predictive Control of Synchronous Reluctance Motor Using Online Parameter Estimation", *Energies*, 13, 492.
- Jackiewicz K. M. (2023), "Sterowanie powtarzalne momentum elektromagnetycznym w układzie napędowym z maszyną reluktancyjną przełączalną", PhD. Diploma thesis, Warsaw University of Technology (in Polish)
- Kumar G.V., Chuang C.H., Lu M.Z, Liaw C.M., (2020) "Development of an Vehicle Synchronous Reluctance Motor Drive", *IEEE Transactions on Vehicular Technology*, vol. 69, pp. 5012–5024, doi:10.1109/TVT.2020.2983546
- Mahmoud, H., Bacco, G., Degano, M., Bianchi, N. and Gerada, C. (2018) "Synchronous Reluctance Motor Iron Losses: Considering Machine Non-linearity at MTPA, FW, and MTPV Operating Conditions," *IEEE Trans. Energy Convers.*, vol. 33, no. 3, pp. 1402–1410, doi: 10.1109/TEC.2018.2811543.
- Manuel, N. and Inanc, N. (2022) "Sliding Mode Control-Based MPPT and Output Voltage Regulation of a Stand-alone PV System", *Power Electronics and Drives*, vol. 7, no. 1, pp. 159–173.
- Niedworok, A. and Orzech, Ł. (2016) "Assessment of efficiency of drive equipped with induction motor and drive equipped with reluctance motor", *Przegląd Elektrotechniczny*, R. 92 NR 8/2016, pp. 246–250 (in Polish).
- Niewiara, Ł.J., Tarczewski, T., Gierczyński, M., Grzesiak, L.M (2023a), „Designing a Hybrid State Feedback Control Structure for a Drive With a Reluctance Synchronous Motor”, *IEEE Trans. on Industrial Electronics*, pp. 1–11, doi:10.1109/TIE.2023.3319726
- Niewiara, Ł.J., Gierczyński, M., Tarczewski, T., Grzesiak, L.M (2023b), „Practical approach for identification and dynamic modeling of reluctance synchronous motors’ electrical circuit”, *The 16th Conference Control in Power Electronics and Electric Drives (SENE 2023)*, Łódź, Poland
- Scokaert, P.O.M. and Mayne, D.Q. (1998) "Min-max feedback model predictive control for constrained linear systems," *IEEE Trans. Automat.*, vol. 43, no. 8, pp. 1136–1142, doi: 10.1109/9.704989.
- Surus, R., Niewiara, L.J., Tarczewski, T., Grzesiak L.M. (2022) "Finite control set model predictive current control for reluctance synchronous motor," in *Proc. IEEE 20th Int. PEMC Conf., Brasov, Romania*, pp. 235–242, doi: 10.1109/PEMC51159.2022.9962908.
- Surus, R., Tejer, M, Niewiara, L.J, Tarczewski, T. (2023) „An Impact of Model Accuracy on Control Performance in Finite Control Set Model Predictive Current Control for Reluctance Synchronous Motor”, *2023 International Conference on Electrical Drives and Power Electronics (EDPE)*, The High Tatras, Slovakia, 2023, pp. 1–7, doi:10.1109/EDPE58625.2023.10274040,
- Sustainable Transport, Electrifying the powertrains of industrial vehicles, transportation and marine - ABB white paper
- Tarczewski, T., Niewiara, Ł. and Grzesiak, L.M, (2021a) "Artificial Neural Network-Based Gain-Scheduled State Feedback Speed Controller for Synchronous Reluctance Motor", *Power Electronics and Drives*, vol. 6, no. 1, pp. 276–288,

- Tarczewski, T., Niewiara, L.J. and Grzesiak, L.M (2021b) "Gain-Scheduled State Feedback Speed Control of Synchronous Reluctance Motor," in Proc. IEEE 19th Int. PEMC Conf., Gliwice, Poland, pp. 559–565, doi: 10.1109/PEMC48073.2021.9432549.
- Wang, F., Mei, X., Rodriguez, J. and Kennel R. (2017) "Model predictive control for electrical drive systems-an overview," CES Trans. on Electrical Machines and Systems, vol. 1, no. 3, pp. 219–230, doi: 10.23919/TEMS.2017.8086100.
- Wang, H. and Zhang, H. (2021) "An Adaptive Control Strategy for a Low-Ripple Boost Converter in BLDC Motor Speed Control", Power Electronics and Drives, vol. 6, no. 1, pp. 242–259.
- Wróbel, K., Serkies, P. and Szabat, K. (2020) "Model Predictive Base Direct Speed Control of Induction Motor Drive-Continuous and Finite Set Approaches", Energies, 13, 1193
- Yamamoto, S., Tomishige, K. and Ara, T. (2005) "A method to calculate transient characteristics of synchronous reluctance motors considering iron loss and cross-magnetic saturation," in Proc. 14th IAS Annual Meeting Conf. IA Conf., Hong Kong, China, pp. 1754–1761 Vol. 3, doi:10.1109/IAS.2005.1518684.
- Yamamoto, Y., Morimoto, S. Sanada, M. Inoue, Y. (2018) "Torque Ripple Reduction Using Asymmetric Flux Barriers in Synchronous Reluctance Motor," in Proc. Int. IPEC-Niigata 2018 -ECCE Asia Conf., Niigata, Japan, pp. 3197–3202, doi: 10.23919/IPEC.2018.8507655.
- Zhang, X., Sun, L., Zhao, K. and Sun, L. (2013) "Nonlinear Speed Control for PMSM System Using Sliding-Mode Control and Disturbance Compensation Techniques," IEEE Trans. Pow. Electron., vol. 28, no. 3, pp. 1358–1365, doi: 10.1109/TPEL.2012.2206610.